A topographic mechanism for arcing of dryland vegetation bands: Supplementary material

Punit Gandhi[*], Lucien Werner[†], Sarah Iams[‡], Karna Gowda[§], Mary Silber[¶]

September 4, 2018

1 Detailed simulation results for topographically extended Klausmeier model

We consider the topographically extended Klausmeier model

$$W_t = T(W) - W - WB^2 + a \tag{1}$$

$$B_t = \nabla^2 B - mB + WB^2, \tag{2}$$

where the water transport is given by

$$T(W) = T_\zeta(W) \equiv \nabla \cdot (W \nabla \zeta). \tag{3}$$

We use the idealized terrain given by

$$\zeta = v(x + \sigma \cos(k_0 y)), \tag{4}$$

fix the plant mortality to $m = 0.45$ [1], and explore the influence of precipitation a and channel aspect σ on patterns within the topographically-extended Klausmeier model. Starting with small ($\sim 5\%$) spatially uncorrelated Gaussian noise on top of a uniformly vegetated initial condition, we integrate forward in time using a fourth order exponential time differencing scheme [2, 3] on an equidistributed mesh. Our calculations are performed in Fourier space and are

[*]Mathematical Biosciences Institute, Ohio State University, Columbus, OH 43210. Email:gandhi.138@mbi.osu.edu

[†]Department of Computing and Mathematical Sciences, California Institute of Technology, Pasadena, CA 91125

[‡]John A. Paulson School of Engineering and Applied Sciences, Harvard University, Cambridge, MA 02138

[§]Department of Physics, University of Illinois at Urbana-Champaign, Urbana IL 61801

[¶]Committee on Computational and Applied Mathematics, and Department of Statistics, University of Chicago, Chicago IL 60637

fully dealiased. We use a periodic domain of $[0, 50] \times [0, 200]$ on a 128×512 grid. We consider our domain to be a small section of a hillslope and therefore employ periodic boundary conditions along the x-direction. While the elevation function ζ in Eq. (4) is not actually periodic along the x-direction because it decreases steadily downslope, the use of periodic boundary conditions is nevertheless readily implemented since only derivatives of ζ appear in Eq. (3).

Generalizations of the Klausmeier model with transport $T^D_{vx}(W) = d\nabla^2(W^\gamma) + vW_x$ that include (potentially nonlinear) water diffusion in addition to the existing advection term in $T^K_{vx}(W)$ allow for pattern formation even when $v = 0$ [4] and lead to spontaneous break-up of stripes on uniformly sloped terrain through secondary instabilities [5]. The Gilad model [6] uses a water transport term of the form $T^G_\zeta(H) = \nabla \cdot (H\nabla(\zeta + H))$ for surface water H, which also includes a nonlinear water diffusion contribution that is not present for $T_\zeta(W)$. In this study, we focus on the influence of topography in the context of banded patterns where water transport is thought to be advection-dominated [7]. We therefore do not expect water diffusion to play an essential role and, indeed, we find that including a (linear or nonlinear) diffusion term in $T_\zeta(W)$ has negligible effect on the results of our simulations provided some biomass is present. Heuristically, one possible danger with not including some form of water diffusion in the model is that water may be able to accumulate in regions of high curvature faster than it can evaporate. However we are modeling water-limited ecosystems and capturing dynamics on time scales of years or longer. Therefore the water input is assumed to be a constant mean value instead of having large spikes corresponding to rain events. In this situation we find that the biomass can effectively use up water and therefore diffuses fast enough to prevent any divergence.

1.1 Arcing of bands in shallow channels

When a small channel aspect ($0 < \sigma \lesssim 0.6$) is taken, simulations produce traveling wave patterns with bands that arc in the same direction as the underlying elevation contours. The straight band traveling solutions shown for the Klausmeier water transport $T^K_{vx}(W) = vW_x$ in Fig. 1(a) become the modulated bands shown in Fig. 1(b) when the topographic extension $T_\zeta(W)$ with $\sigma = 0.5$ is used. While the bands are modulated such that the arcing-direction matches the direction of curvature of the underlying terrain along ridges and valleys, the vegetation bands do not closely match the contour lines shown superimposed on the water field W. There is only a slight curvature of the contour lines in Fig. 1(b) while the bands are noticeably more arced.

We also consider an alternate extension to the Klausmeier transport $T^K_\zeta(W)$ that includes only the advection term of Eq. (3). We find that this advection-only transport,

$$T^A_\zeta(W) = \nabla\zeta \cdot \nabla W, \quad \zeta = v(x + \sigma\cos(k_0 y)), \tag{5}$$

does not produce arced vegetation bands. Figure 1(c) shows the result of a simulation initialized with arced vegetation bands from Fig. 1(b) and using the

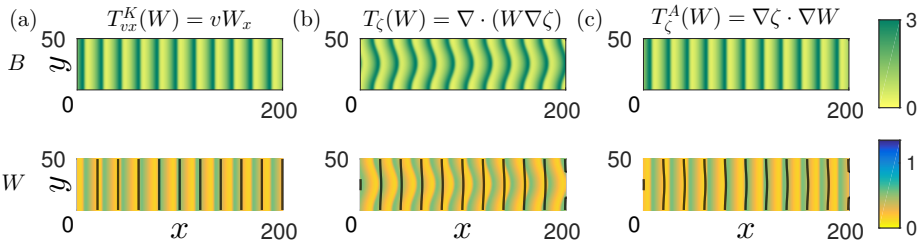


Figure 1: Biomass (B) and water (W) at $t = 1000$ from a simulation of the Klausmeier system, Eqs. (1)-(2), (a) initialized with uniform vegetation and small noise using $T^K_{vx}(W) = vW_x$ and (b) $T_\zeta(W) = \nabla \cdot (W\nabla\zeta)$ where $\zeta = v\,(x + \sigma\cos(k_0 y))$. The solution shown in (b) is taken as initial condition for a simulation using $T^A_\zeta(W) = \nabla\zeta \cdot \nabla W$ and the result at $t = 1000$ is shown in (c). For each case black lines of constant elevation (straight in (a) and slightly curved in (b,c)) are superimposed on W. If the $W\nabla^2\zeta$ term is neglected from $T_\zeta(W)$, then the simulation tends to straight vegetation bands shown in (c). The simulations are carried out on a periodic domain of size 200×50 with parameters $a = 0.95$, $v = 10$, $m = 0.45$, $\sigma = 0.5$, $k_0 = 2\pi/50$.

transport $T^A_\zeta(W)$ above. The initially curved vegetation bands straighten out to become the y-independent solution of the original Klausemeier model shown in Fig. 1(a). The persistence of this straight-band solution in the presence of the advection-only transport $T^A_\zeta(W)$ for $\sigma \neq 0$ can be understood as follows. A y-independent solution to the original Klausmeier system with transport $T^K_{vx}(W)$ will also be a solution to the system with advection-only transport $T^A_\zeta(W)$. This is because $\nabla W = W_x\hat{\mathbf{x}}$ if $W_y = 0$, and so $T^A_\zeta(W) = T^K_{vx}(W)$ for y-independent W. Thus the solution with straight bands aligned along y continues to exist, and numerical simulations (Fig. 1(c)) indicate that this straight-band solution not only remains stable for $\sigma \neq 0$, but is actually a preferred solution in this example.

1.2 Classifying patterns on ridges and in valleys

Figure 2 shows snapshots of biomass (at $t = 1000$) from simulations along with elevation contours for various values of precipitation a and channel aspect ratio σ that illustrate qualitatively different patterns predicted by the model. We choose a precipitation value ($a = 0.95$) for which stable traveling waves of banded vegetation moving uphill exist on a uniformly sloped terrain ($\sigma = 0$ as in Fig. 1(a)) and introduce a curvature in elevation transverse to the slope ($\sigma > 0$). As noted in Sec. 1.1, e.g., $\sigma = 0.5$ in Fig. 1(b), the asymptotic state remains a traveling wave with velocity directed uphill for small aspect ratio σ, but the bands are arced convex-upslope within valleys and convex-downslope on top of ridges.

For $\sigma = 2$, shown in Fig. 2(b), the simulation produces a periodic pattern

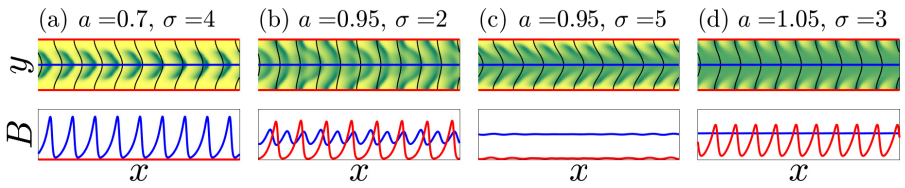


Figure 2: Qualitatively different patterns as a function of the parameters (a, σ). Biomass is shown at t=1000 from simulations with (a) $a = 0.70$ and $\sigma = 4$, (b) $a = 0.95$ and $\sigma = 2$, (c) $a = 0.95$ and $\sigma = 5$, and (d) $a = 1.05$ and $\sigma = 3$. For each case, the upper image shows the biomass on the full 2D domain while the lower image shows profiles of the biomass along the ridge (red) and valley (blue). Simulations are initialized with small noise on top of a uniformly vegetated state and carried out on a periodic domain of size 200×50 with parameters $v = 10$, $m = 0.45$, $k_0 = 2\pi/50$.

with a wavelength that is 1.5 times longer on the ridges than in the valleys. The speed of the pattern on ridges is slower than within valleys, resulting in phase slips in which bands extending across the ridges and valleys break apart into arced segments and reconnect with other arced segments to form new bands that extend across the domain. We note that the speed can be either faster or slower in a valley, depending on parameters and the ratio of wavelengths. When the wavelengths are the same, as is the case when $\sigma = 1$ and $a = 0.95$ (not shown), we find that the pattern in the valleys moves faster than the pattern on the ridges. When the wavelengths are different, we find cases (e.g., $\sigma = 2$ and $a = 0.95$ shown in Fig. 2(b)) where the longer wavelength pattern on ridges moves faster than the shorter wavelength pattern in valleys. Such behavior is not unexpected based on trends of linear theory: the speed of uphill migration computed from linearization about the uniform state increases with increasing wavelength and decreases with increasing water loss rate when all other parameters are fixed [8]. Eventually, for large enough aspect σ, nearly uniform vegetation cover develops within valleys while ridges becomes nearly bare (for example $\sigma = 5$ in Fig. 2(c)). In this case the vegetation bands are restricted to the channel walls between the valley and ridge lines, forming chevrons.

1.3 Mapping out patterns in the (a, σ)-plane

We map out the existence of patterned states of the topographically-extended Klausmeier model in the (a, σ)-plane by scanning over the precipitation parameter a for fixed values of channel aspect σ as described below. We initialize each simulation with a uniformly vegetated state at a high enough precipitation value a so as to ensure that a state consisting of uniform vegetation cover on both ridges and valleys is stable at the given value of σ. For each fixed channel aspect σ, we decrease the value of a at a rate $da/dt = -5 \times 10^{-5}$, adding 1% spatially

uncorrelated Gaussian noise to the solution at time intervals of $\Delta t = 100$. As a check for hysteresis, at each fixed value of σ we also run the simulation for increasing precipitation ($da/dt = +5 \times 10^{-5}$) starting from the last value of a before the vegetation in the system collapses to the bare soil state.

We consider biomass profiles along the ridge $B_R(x) = B(x, y = 0)$ and the valley ($B_V(x) = B(x, y = L/2)$ (red and blue profiles in Fig. 2) for a grid in the (a, σ) plane with spacing $\Delta a = 0.01$, $\Delta\sigma = 0.5$. At each point on the parameter grid, the pattern amplitude along the ridge (R) and valley (V) lines is computed via $A_{R,V} = \max_x(B_{R,V}(x)) - \min_x(B_{R,V}(x))$. Because of hysteresis, the amplitudes $A_{R,V}$ may be different for the decreasing and increasing a portions of the simulation at a given point in parameter space. We are interested in mapping out the parameter region of existence for patterns so we take the maximum of $A_{R,V}$ between the increasing and decreasing a cases, whenever a difference can be computed.

Figure 3(a) shows the maximum ridge (valley) pattern amplitudes A_R (A_V) in red (blue) at each point in the (a, σ)-plane. Purple indicates where patterns appear on both ridges and valleys while yellow indicates where no significant pattern amplitudes appear on either ridges or valleys. The visualization of the data in Fig. 3(a) does not distinguish between uniform vegetation cover and bare soil so we additionally label each region of the parameter space based on the ridge and valley states. The algorithm for obtaining the amplitude is illustrated for $\sigma = 2.5$ (see dashed gray line) in the right panels. Figure 3(b) shows $\max_x(B(x))$ (solid) and $\min_x(B(x))$ (dotted) as the parameter a is decreased for $y = 0$ (red), corresponding a ridge, and for $y = L_y/2$ (blue), corresponding to a valley. The pattern amplitude, computed by taking the difference, $A = \max_x(B(x)) - \min_x(B(x))$, are shown for ridge (red) and valley (blue) in Fig. 3(c). Here the solid line represents the pattern amplitude as a is decreased and the dotted line represents the pattern amplitude as a is increased. The shaded regions in panels (b) and (c) represent the predictions for the existence of patterns from the one-dimensional model for the ridge (red) and the valley (blue).

2 Simulation results from a three-field model

We have partially mapped out the influence of terrain curvature as a function of water input using a three-field model that subdivides water into a surface water field H and a soil moisture field W. The model we use, a simplified version of the Gilad model [6], takes the form:

$$H_t = p - I + D_h\nabla^2 H + \nabla\zeta \cdot \nabla H + (\nabla^2\zeta)H \tag{6}$$

$$S_t = I - \nu S(1 - \rho B) - \gamma G_w \tag{7}$$

$$B_t = -mB + \nu G_w(1 - B) + D_b\nabla^2 B \tag{8}$$

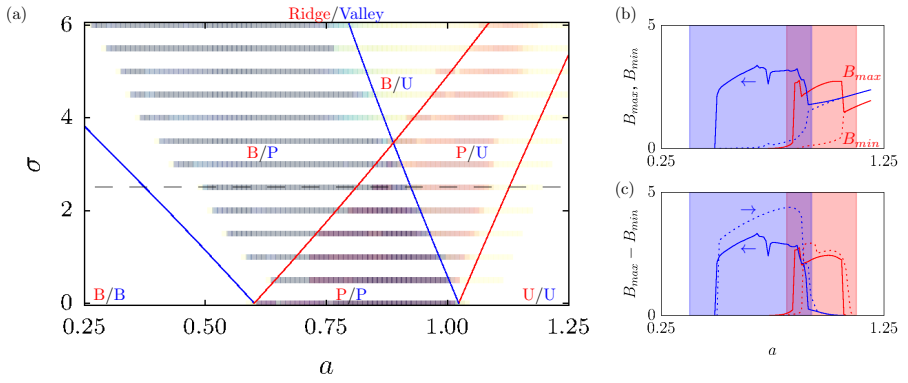


Figure 3: (a) Maximum of amplitude of patterns on ridge (red) and valley (blue) in (a, σ) plane when a is decreased and then increased for fixed σ. Yellow indicates small amplitude while red (blue) indicates large amplitude on ridge (valley) and purple indicates large amplitude on ridge and in valley. Solid red (blue) lines show predicted transitions between regions of parameter from the one-dimensional approximation for the ridges (valleys). Each region is labeled by ridge/valley state as bare soil (B), patterned (P) or uniformly vegetated (U). (b) Profiles of $\max_x(B)$ (solid) and $\min_x(B)$ (dotted) along the ridge (red) and valley (blue) are shown for decreasing a for fixed $\sigma = 2.5$ (dashed line in (a)). (c) Profiles of pattern amplitude $A = \max_x(B) - \min_x(B)$ along ridge (red) and valley (blue) for a decreasing (solid) and increasing (dotted) at fixed $\sigma = 2.5$. The shaded regions in (b) and (c) indicate values of a where the one-dimensional approximation predicts patterns to exist on the ridge (red) and in the valley (blue). Parameters: $m = 0.45$, $v = 10$, $k_0 = 2\pi/50$.

where infiltration and transpiration functions are given by

$$I = \alpha H \frac{B + qf}{B + q}, \qquad G_w = WB(1 + \eta B)^2 \tag{9}$$

and the elevation function is

$$\zeta = v\,(x + \sigma \cos(k_0 y)) \tag{10}$$

The parameter values used for the simulations are: $D_b = 1$, $D_h = 10$, $v = 50$, $\nu = 3.33$, $\rho = 0.95$, $m = 1.0$, $\gamma = 16.66$, $\alpha = 33.3$, $q = 0.05$, $f = 0.1$, $\eta = 3.5$.

Figure 4 summarizes the results of these simulations carried out on a two-dimensional domain in the (p, σ)-plane. The patterns generated from the simulation, once classified in terms of ridge/valley vegetation state, reveals a qualitatively similar parameter space structure as seen for the topographically extended Klausmeier model in Fig. 3. While we do not present numerical continuation results of a one-dimensional Gilad model, the structure of the equations allows

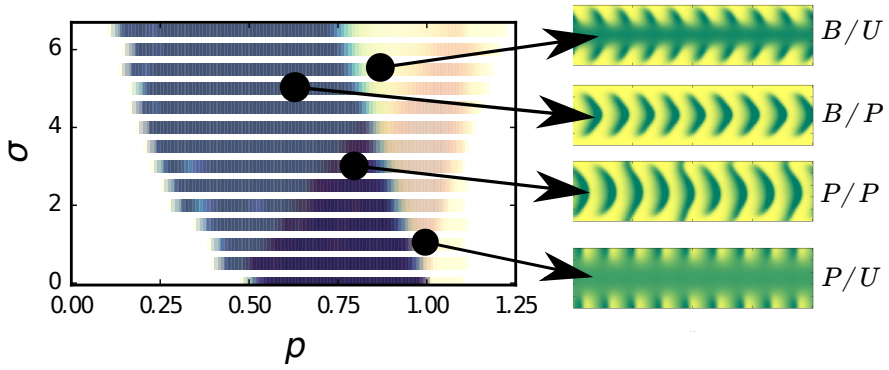


Figure 4: Simulation results based on a local approximation to the Gilad model using an idealized terrain consisting of a periodic array of ridges and valleys aligned along a hillslope. The precipitation level is characterized by p and the terrain curvature is parametrized by σ. Left panel: Colors indicate the ridge/valley state observed from numerical simulation for a given precipitation p and terrain curvature σ. Blue: B/P, Red: P/U, Purple: P/P, and Yellow: B/U or U/U. Right Panels: Example biomass profiles for pattern types appearing in the simulation.

us to interpret terrain curvature as effectively changing water loss rate in the equation for surface water H in a similar way as was done for the equation for water W in the Klausmeier model. Because the surface water is diverted from ridges and accumulates in valleys, we see an increased infiltration and thus increased level of soil moisture in valleys relative to ridges.

References

[1] C. A. Klausmeier. Regular and irregular patterns in semiarid vegetation. *Science*, 284(5421):1826–1828, 1999.

[2] S. M. Cox and P. C. Matthews. Exponential time differencing for stiff systems. *J. Comp. Phys.*, 176(2):430–455, 2002.

[3] A. Kassam and L. N Trefethen. Fourth-order time-stepping for stiff PDEs. *SIAM J. Sci. Comp.*, 26(4):1214–1233, 2005.

[4] S. van der Stelt, A. Doelman, G. Hek, and J. D. M. Rademacher. Rise and fall of periodic patterns for a generalized Klausmeier–Gray–Scott model. *J. Nonlin. Sci.*, 23(1):39–95, 2013.

[5] E. Siero, A. Doelman, M. B. Eppinga, J. D. M. Rademacher, M. Rietkerk, and K. Siteur. Striped pattern selection by advective reaction-diffusion

systems: Resilience of banded vegetation on slopes. *Chaos*, 25(3):036411, 2015.

[6] E. Gilad, J. von Hardenberg, A. Provenzale, M. Shachak, and E. Meron. Ecosystem engineers: from pattern formation to habitat creation. *Phys. Rev. Lett.*, 93(9):098105, 2004.

[7] C. Valentin, J.-M. d'Herbès, and J. Poesen. Soil and water components of banded vegetation patterns. *Catena*, 37(1-2):1–24, 1999.

[8] J. A. Sherratt. An analysis of vegetation stripe formation in semi-arid landscapes. *J. Math. Biol.*, 51(2):183–197, 2005.